Journal of Nuclear Materials 396 (2010) 1–9

Contents lists available at ScienceDirect

Journal of Nuclear Materials

journal homepage: www.elsevier.com/locate/jnucmat

Analysis of tensile deformation and failure in austenitic stainless steels: Part I – Temperature dependence

Jin Weon Kim [a], Thak Sang Byun [b,*]

[a] Department of Nuclear Engineering, Chosun University, 375 Seosuk-dong, Dong-gu, Gwangju 501-759, Republic of Korea
[b] Oak Ridge National Laboratory, Material Science and Technology Division, P.O. Box 2008, MS-6138, Oak Ridge, TN 37831, United States

A B S T R A C T

This paper describes the temperature dependence of deformation and failure behaviors in the austenitic stainless steels (annealed 304, 316, 316LN, and 20% cold-worked 316LN) in terms of equivalent true stress–true strain curves. The true stress–true strain curves up to the final fracture were calculated from tensile test data obtained at −150 to 450 °C using an iterative finite element method. Analysis was largely focused on the necking and fracture: key parameters such as the strain hardening rate, equivalent fracture stress, fracture strain, and tensile fracture energy were evaluated, and their temperature dependencies were investigated. It was shown that a significantly high strain hardening rate was retained during unstable deformation although overall strain hardening rate beyond the onset of necking was lower than that of the uniform deformation. The fracture stress and energy decreased with temperature up to 200 °C and were nearly saturated as the temperature came close to the maximum test temperature 450 °C. The fracture strain had a maximum at −50 to 20 °C before decreasing with temperature. It was explained that these temperature dependencies of fracture properties were associated with a change in the dominant strain hardening mechanism with test temperature. Also, it was seen that the pre-straining of material has little effect on the strain hardening rate during necking deformation and on fracture properties.

Published by Elsevier B.V.

1. Introduction

The deformation and fracture behaviors of highly ductile 300 series stainless steels (SSs) can be significantly changed by material and testing conditions such as test temperature, irradiation, and pre-deformation. A systematic explanation for the changes has often been limited because most of the studies focused on the uniform deformation only and the details of the later part of deformation, or necking deformation, was largely ignored [1,2]. In the metallic materials the total necking strain can be much higher, along with higher stress level, than the strain achievable from the uniform deformation [3]. It is expected that the unit volume of a metallic material can absorb more energy in unstable (or necking) deformation than in uniform deformation. The unstable deformation is particularly important in the materials irradiated to high doses, where the onset of necking occurs at yield but a significant true necking strain can be obtained [4–6]. In such cases, the unstable deformation occupies the major part of the whole deformation and the failure properties obtained from true stress (σ_T)–true strain (ε_T) relation during unstable deformation can be the only information to describe the mechanical behavior of the material. It is therefore recognized that obtaining the full true stress–true strain data up to the final fracture, including the unstable deformation, is important to thoroughly understand the true characteristics of materials.

This study aimed at detailed investigations on the temperature dependence of deformation and failure behaviors in the austenitic stainless steels in terms of the true stress–true strain curves covering both uniform and unstable deformation. Several experimental methods for finding true stress–true strain relation beyond the onset of necking, *i.e.*, Bridgeman's method and grid method, have been suggested [7,8]. However, there are some limitations to practically apply these methods: For Bridgeman's method, its application is limited to round bar specimens because it cannot consider the complicated necking behavior of flat specimens that often show a necking mode transition during unstable deformation [9]. Grid method is also complicated for practical uses because the deformation pattern of grid lines on the surface of specimen cannot be monitored accurately during necking at the minimum cross-section of specimen [9]. To exclude such limitations in experimental methods, a simple approximation method based on a linear strain hardening model for unstable deformation has been suggested and applied to irradiated materials [3,10–12]. However, this model can provide nominal true stress value only instead of equivalent true stress which is a more genuine stress response of the

* Corresponding author. Tel.: +1 865 576 7738.
E-mail address: byunts@ornl.gov (T.S. Byun).

0022-3115/$ - see front matter Published by Elsevier B.V.
doi:10.1016/j.jnucmat.2009.08.010

material and is nearly independent of specimen geometry [13]. Recently, the finite element (FE) simulation method has been used as an alternative way to get the full true stress–true strain curve including unstable deformation [14–16]. It is known that the method can accurately simulate necking phenomena and give reliable equivalent true stress–true strain curve from the tensile data given by flat specimens as well as by round bar specimens [16–18]. In recent years the long computation time, which has been a main short coming for detailed FE calculations, was significantly reduced [9,19]. Another key merit of the FE analysis is that all stress and strain components can be determined for the necking deformation where multi-axial stress and strain fields develop.

The 300 series (austenitic) stainless steels have been commonly used in nuclear facilities such as fission reactors, spallation neutron sources, and fusion test reactors. Thus, extensive tensile data for various test and irradiation conditions have been accumulated in the past. Using iterative finite element simulations, therefore, this study attempts to obtain full equivalent true stress–true strain curves including unstable deformation for those austenitic stainless steels. The ABACUS program was used for all FE simulations, and the simulation results include the strain hardening properties for unstable deformation and tensile fracture properties, *i.e.*, equivalent fracture stress (σ_{FE}), fracture strain (ε_F), and tensile fracture energy (E_F). The part I paper provides the full equivalent true stress–true strain curves for the four austenitic stainless steels tested at various test temperatures and discusses the temperature dependencies of strain hardening behavior during unstable deformation and fracture properties for austenitic stainless steels. In the Part II paper the irradiation dose dependencies of strain hardening behavior during unstable deformation and fracture properties are discussed based on the calculated true stress–true strain curves.

2. Tensile data for analysis

Tensile data (UI1–UI4) produced in earlier studies were used to generate full range true stress–true strain curves for four 300 series austenitic stainless steels: annealed 304, 316, 316LN, and 20% cold-worked (CW) 316LN SSs, tested over the temperature range from −150 °C to 450 °C [20]. Table 1 summarizes the chemistry and thermo-mechanical history for the materials. A subsized flat specimen with the gage section of $7.62 \times 1.52 \times 0.76$ mm (SS-3 type specimen) was used for the tensile tests. Tests were conducted using a screw-driven machine at a nominal strain rate of about 10^{-3} s^{-1}. Test temperatures ranged from −150 to 400 or 450 °C, and were controlled by an automatic heating/cooling chamber system using electrical heating and liquid nitrogen cooling. Fig. 1 shows the engineering stress–strain curves of the materials at each test temperature considered in the present study. As shown in Fig. 1, the engineering stress–strain curves showed different patterns depending on test temperature and cold-working.

3. Simulation procedure and finite element model

3.1. Equivalent true stress–true strain calculation procedure

This calculation procedure includes steps for uniform deformation and unstable plasticity regimes in tensile deformation. For both regimes, the ABACUS program uses the traditional definitions for the equivalent true stress and true strain:

$$\sigma_T = \frac{1}{\sqrt{2}}\left[(\sigma_1-\sigma_2)^2+(\sigma_2-\sigma_3)^2+(\sigma_3-\sigma_1)^2\right]^{1/2}, \quad (1)$$

$$\varepsilon_T = \frac{\sqrt{2}}{3}\left[(\varepsilon_1-\varepsilon_2)^2+(\varepsilon_2-\varepsilon_3)^2+(\varepsilon_3-\varepsilon_1)^2\right]^{1/2}, \quad (2)$$

where σ_1 and ε_1 denote the principal stress and strain components in the tensile (axial) direction and σ_2, σ_3, ε_2 and ε_3 are those in the two perpendicular (width and thickness) directions. Since the stress and strain in tensile tests are in a uniaxial stress state before the onset of necking, the equivalent true stress–true strain relation to the onset of necking can be directly obtained from the experimental load (F)–displacement (δ) data using the following Eqs. (3) and (4):

$$\sigma_T = \sigma_1 = \frac{F}{A_o}\left(\frac{\delta}{L_o}+1\right), \quad (3)$$

$$\varepsilon_T = \varepsilon_1 = \ln\left(\frac{\delta}{L_o}+1\right), \quad (4)$$

where A_o is the initial cross-sectional area of specimen and L_o is the initial gage length.

After the onset of necking the deformation becomes three dimensional, and the perpendicular stress and strain components cannot be directly obtained from the load–displacement measurements. In the present procedure, therefore, the equivalent true stress–true stain curve for the necking deformation is obtained using an iterative calculation technique. In this technique the experimental load–displacement curve is considered as a target output and the input, the true stress–true strain data, to produce the target is repeatedly updated for iterative calculations. In order to reduce the number of iterations, this study employed a simplified iteration procedure based on the existing studies [14,19], which consists of the following steps:

(i) Calculate the true stress–true strain curve up to necking from load–displacement data using Eqs. (3) and (4), and extrapolate the curve after necking using a power law fit.
(ii) Perform a finite element simulation for a load (F_i) and displacement dataset (δ_i) considering the actual dimension of each specimen with the true stress–true strain obtained by step (i), and compare the calculated load–displacement response with the experimental measurements. Calculate the relative error of the load (ΔF_i) at the given displacement (δ_i), where ΔF_i is the difference between the measured load (F_m) and the calculated load (F_i).

Table 1
Materials and heat-treatments [1].

Data ID	Materials	Chemical compositions (wt.%)	Heat treatment	Test temperature (°C)
UI1	304-Annealed	Fe-18.37Cr-8.04Ni-0.04Mo-1.73Mn-0.44Si-0.022P-0.036C-0.058N-0.1Cu-0.12V-0.03Co	Annealed at 1050 °C for 30 min	−150 to 400
UI2	316-Annealed	Fe-17.15Cr-13.45Ni-2.34Mo-1.86Mn-0.57Si-0.024P-0.059C-0.031N-0.018S-0.1Cu-0.02Co	Annealed at 1050 °C for 30 min	−150 to 450
UI3	316LN-Annealed	Fe-16.3Cr-10.2Ni-2.01Mo-1.75Mn-0.39Si-0.029P-0.009C-0.11N	Annealed at 1050 °C for 30min	−150 to 400
UI4	316LN-20% CW	Fe-16.3Cr-10.2Ni-2.01Mo-1.75Mn-0.39Si-0.029P-0.009C-0.11N	Annealed at 1050 °C for 30 min and 20% cold-rolled	−150 to 400

(iii) Adjust the true stress–true strain curve for necking deformation based on ΔF_i obtained in step (ii) using Eq. (5) and replace the true stress–true strain curve with the updated one ($\sigma_i - \varepsilon_i$).

$$\sigma_i = \sigma_{i,o} + \sigma_{i,o}\left(\frac{\Delta F_i}{F_i}\right), \tag{5}$$

where σ_i and $\sigma_{i,o}$ are the updated and current true stresses at ε_i corresponding to a displacement of δ_i. Here, the true strain during unstable deformation, ε_i, is defined as the average axial strain in the smallest cross-section of neck and is expressed as

$$\varepsilon_i = \ln\left(\frac{A_o}{A_i}\right), \tag{6}$$

where A_o is the initial cross-section of specimen and A_i is the predicted cross-section of necking at the displacement (δ_i).

Repeat the steps (ii) and (iii) until the relative error reaches a specified tolerance and take the finally updated $\sigma_i - \varepsilon_i$ as the true stress–true strain curve of the material. Thus, the curve for necking deformation obtained by this procedure is the equivalent true stress–true strain curve under multi-axial stress state.

In each incremental step, the experimental load–displacement data, which can be easily converted from the engineering stress–strain curves in Fig. 1, were used as the boundary conditions for force and displacement in the one-eighth model, Fig. 2. The amount of specimen extension was applied to the artificial node in Fig. 2 as a displacement boundary condition. The force calculated at the artificial node in the end of iterative calculations should satisfy the boundary condition: the force value from the experimental flow curve at a given elongation.

In the FE simulation, the calculated load–displacement curve beyond the onset of necking considerably changed with the true stress value in the strain range just after the onset of necking, whereas it was less sensitive to the true stress values at higher strain region. Thus, the determination of accurate true stress–true strain curve just after the onset of necking is important. In this study the iteration was continued until the experimental and calculated load–displacement curves were almost completely matched around the onset of necking, although the overall error satisfied the specified tolerance.

It is known that the strain distribution in a tensile specimen is highly heterogeneous around the smallest cross-section during necking [9,14,15]. For the thin flat samples, in particular, it is unlikely to accurately estimate the true strain at the point of final failure from the simulation since the local strain increases very rapidly and the final fracture occurs in the end of localized necking [9,16]. In this simulation, therefore, the average values of fracture parameters were evaluated, ignoring variations within the minimum cross-sectional area; for example, the equivalent fracture strain was determined from the simulated cross-section area (A_F) at the displacement corresponding to final failure (δ_F) in the load–displacement curve [9]. For each case, the equivalent true stress–true strain curve was calculated up to the final catastrophic fracture point detected in the experimental load–displacement curve. It is worth noting that the plastic deformation behaviors of a material are different for different geometries or constraints, and therefore the basic hypotheses used in this analysis are considered to be limited to the static uniaxial tensile testing for flat specimens.

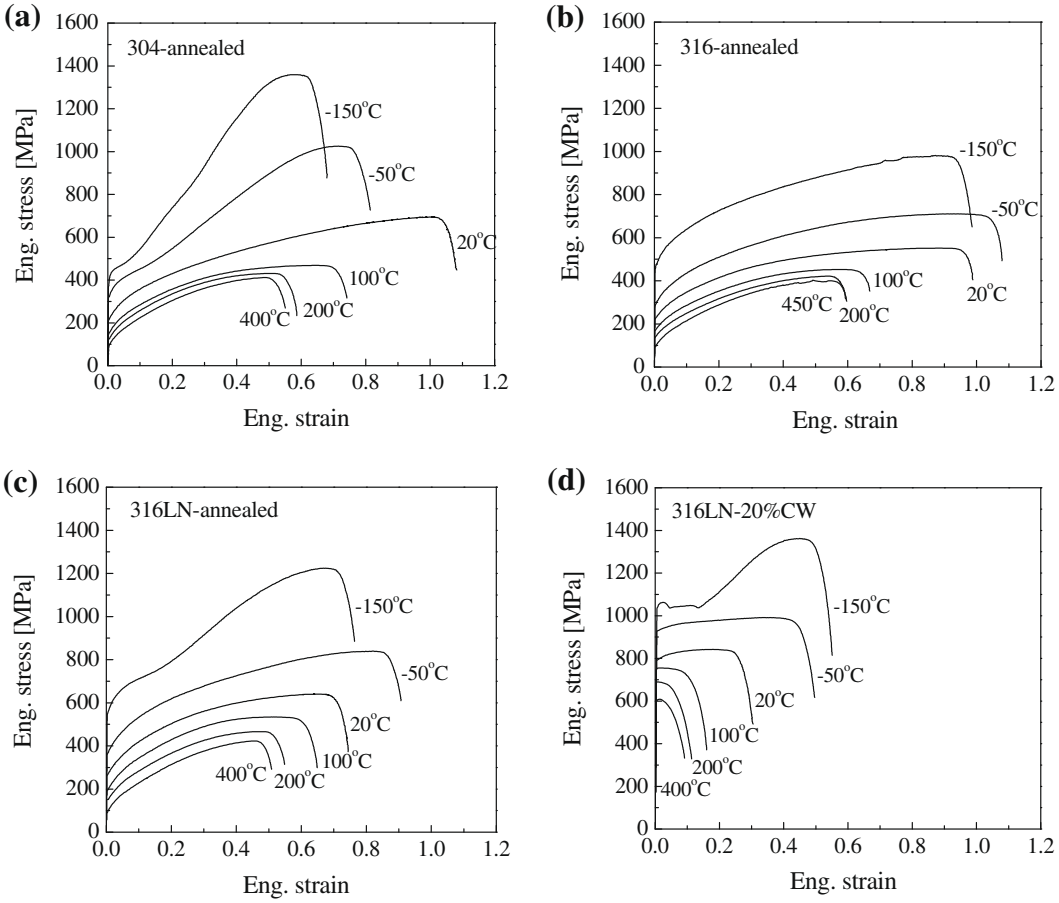

Fig. 1. Engineering stress–strain curves for austenitic stainless steels: (a) 304-annealed, (b) 316-annealed, (c) 316LN-annealed, and (d) 316LN-20% cold-worked steels [1].

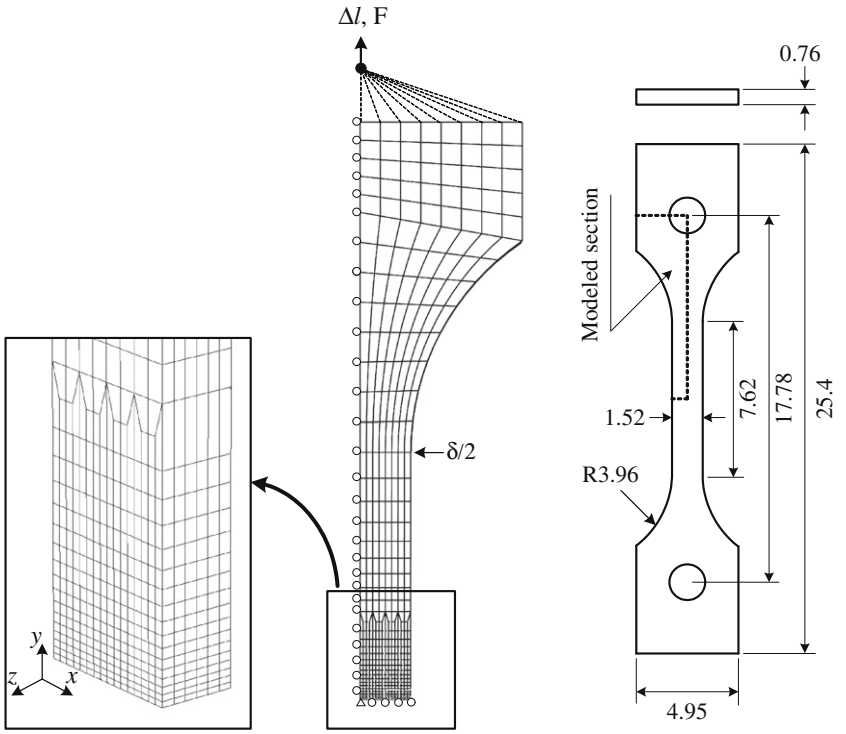

Fig. 2. Finite element model used for the simulation of tensile test.

3.2. Finite element models

Finite element simulation of tensile tests was performed using a general-purpose finite element program, ABAQUS [21]. To simulate shear deformation in the width direction and thinning in the thickness direction in the localized necking area, three-dimensional models using twenty-node solid element with reduced integration (C3D20R in ABAQUS) were used in the simulation. Considering the symmetry of specimen shown in Fig. 2, one eighth of the full specimen including a section of specimen head was modeled. Finer meshes were modeled near the center of the specimen where the strain gradient was expected to be large; at the center of the specimen sixteen and six elements were layered in the width and thickness directions, respectively. The number of elements and the element sizes were optimized based on the convergence test. Material and geometrical nonlinearities were considered in the analyses to properly simulate the necking of specimens: Materials were modeled as isotropic elastic-plastic materials that obey the incremental plasticity theory. The nonlinear geometry option (NLGEOM) in the ABAQUS program was chosen to incorporate large geometry changes.

To induce an initiation of necking in the simulation, a geometrical imperfection in a form of locally reduced width and thickness by 0.25% from their nominal dimensions was assumed to be embedded in the central elements of specimen in the finite element model. The degree of geometrical imperfection was determined based on the manufacturing tolerance in specimen dimensions as well as on the result from a sensitivity analysis using the ABAQUS program for the SS-3 specimen geometry. The 0.25% imperfection was enough to induce a necking but was less than the usual manufacturing tolerance for such tensile specimens (5 μm). Also, embedding the imperfection in the geometrical symmetry point of specimen reduced significant computation time [14–17]. The necking patterns are discussed in a following section.

3.3. Verification of finite element simulation

In each simulation the experimental load–displacement curve was used not only as the target in iterative calculation but also as a measure to validate the finite element model. In all cases, the predicted and measured loads and displacements at the onset of necking were almost identical. It was also possible to almost completely match the simulated load–displacement curve with the experimental one for the necking deformation up to the final failure, except for a minor difference displayed for some high temperature cases. Fig. 3 shows the selected cases for load–displacement curve comparison.

The strain contour and deformation patterns at the point of final failure were examined to check if the use of the same FE model and calculation scheme is reasonable for the whole deformation. As seen in Fig. 4, the higher level of maximum principal logarithmic strain (true strain) appeared at the center of the cross-section and its contour spreads along the perpendicular plane. Such an asymmetrical contour pattern at final failure can be observed in flat specimens when the test material is highly ductile [3]. According to some earlier studies [17,18], the transition from diffuse to localized necking mode occurs when the aspect ratio of gage section (=the width-to-thickness ratio) is 3 – 6, depending on the mechanical property of the material. The aspect ratio tends to increase as the plastic deformation progresses because the straining in the thickness direction is slightly preferred in flat specimens. For the SS-3 type specimens, since the initial aspect ratio of cross-sectional area is about 2, relatively short localized necking occurred before the final fracture. It is believed that the current FE analysis effectively simulates the unstable deformation behavior during necking in flat specimens.

It is also worth recognizing that, although the continuum theory-based FE models cannot simulate the microstructural failure mechanisms such as void nucleation, growth, and coalescence, the final portions of the experimental engineering stress–strain

curves included in the simulation reflect the early part of the final failure process. In the formation of a localized neck, in particular, a ductile micro-fracture mechanism might operate within the shear band and its effect should be reflected as a steep decrease of load in the experimental curves. In this study, the final deformation mode was mostly localized necking, i.e., shear band formation, and FE simulation was performed until the load starts to drop catastrophically. At least the earlier portion of the final fracture process was therefore reflected in the simulation results: the effect of void formation may appear as a reduced strain-hardening rate in the end portions of the true stress–true strain curves by this method, if any. However, since the total void volume is believed to be small in the shear-dominant neck of austenitic stainless steels, the effect from such phenomenon should be negligible before the final catastrophic fracture, which cannot be simulated in this study.

4. Results and discussion

4.1. Equivalent true stress–true strain curves

The equivalent true stress–true strain curves including unstable deformation for the four austenitic stainless steels, annealed 304, 316, 316LN, and 20% CW 316LN, tested at different temperatures were determined using finite element simulations. In all test materials, as shown in Fig. 5, it is seen that the equivalent true stress after the onset of necking still increased with increasing true strain without any discernable transition in the curves, although the slope of the curves decreased. As the test temperature increased, the hardening rate in equivalent true stress term during unstable deformation was considerably reduced and became negligible above 200 °C, while the continuity of the curves at the onset of necking was still kept. These results indicate that either the same strain hardening mechanism is still operative in the unstable deformation or the change in the mechanism, if any, is gradual. It is also worth noting that the same characteristics of unstable deformation were observed for the 20% CW 316LN SS and annealed stainless steels.

Fig. 6 compares the equivalent true stress–true strain curves of annealed 316LN SS and 20% CW 316LN SS. To compare the strain hardening behaviors in unstable deformation regime, the effect of pre-straining was excluded by shifting the curves of 20% CW 316LN SS along the strain axis. It is shown that the equivalent true stress–true strain curves beyond the onset of necking for the 20% CW 316LN SS are superimposed well on the curves for annealed 316LN SS except for the case of 100 °C test. In the uniform deformation regime, in general, the strain hardening rate of materials is not changed by cold-working [13]. Fig. 6 confirms that the validity of such strain hardening characteristics can be extended to the

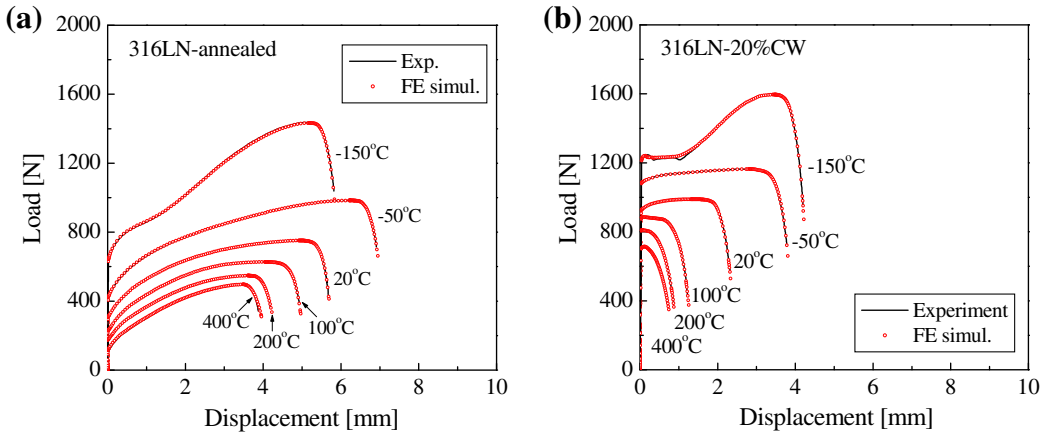

Fig. 3. Comparisons of load–displacement curves obtained from experiment and finite element simulation: for (a) 316LN-annealed and (b) 316LN-20% cold-worked conditions.

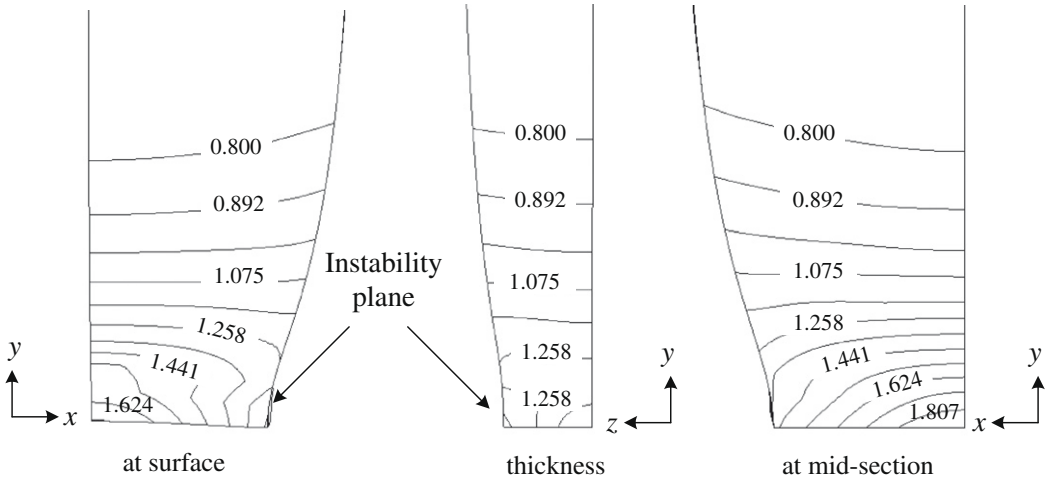

Fig. 4. Deformation patterns and distributions for the maximum principle logarithmic strain at final failure.

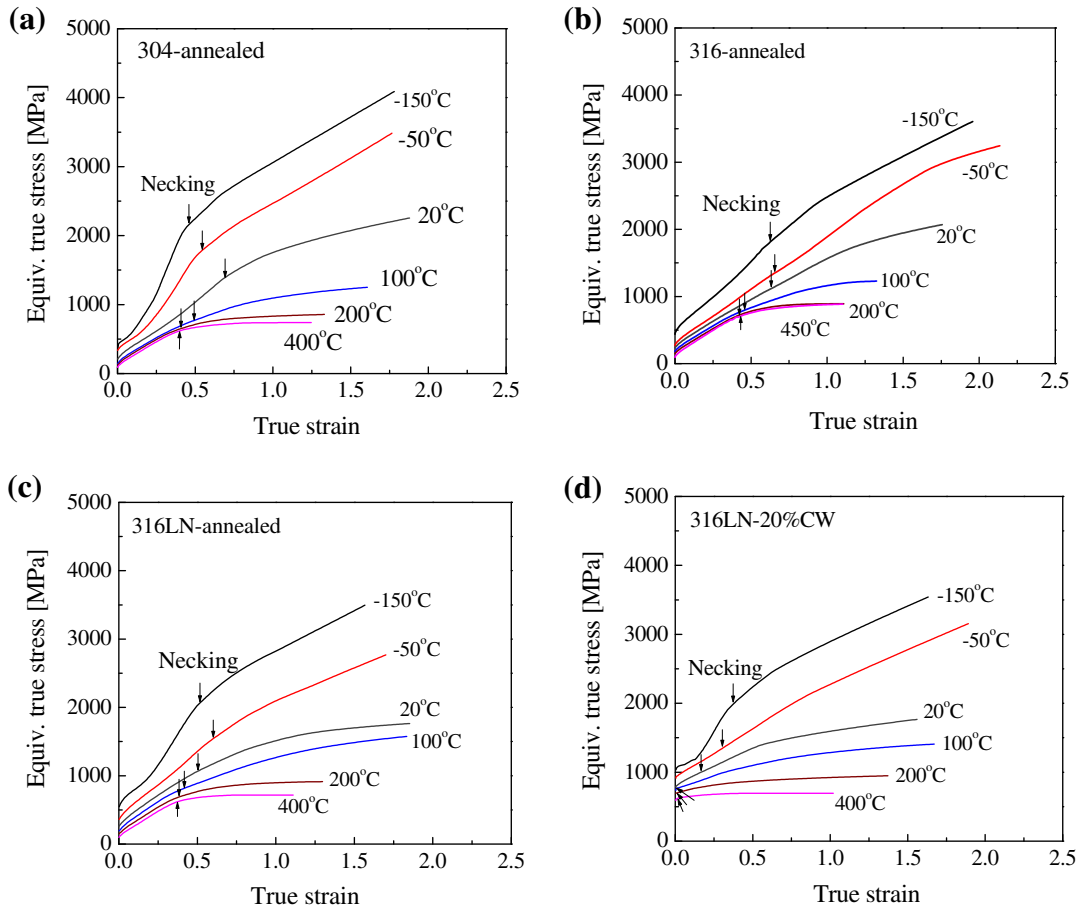

Fig. 5. Equivalent true stress–true strain curves for austenitic stainless steels at various temperatures: for (a) 304-annealed, (b) 316-annealed, (c) 316LN-annealed, and (d) 316LN-20% cold-worked steels.

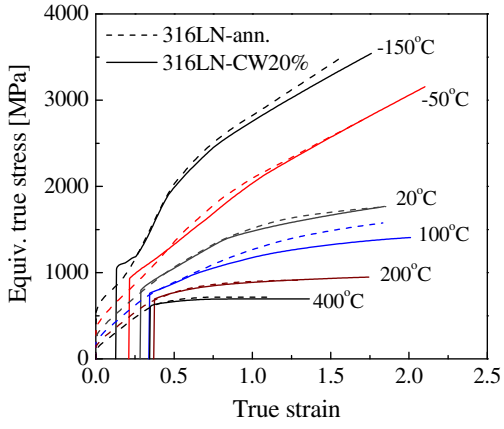

Fig. 6. Comparisons of true stress–true strain curves for 316LN stainless steel in annealed and 20% cold-worked conditions.

unstable deformation regime. That is, the strain hardening rate during unstable deformation is little affected by pre-straining of materials.

Also seen in Fig. 6 is that the strain shift is different for different test temperatures even though all specimens were subjected to the same level of pre-straining, 20% CW. The shift was less than 20% for the test temperatures of −150 and −50 °C and higher than 20% for the test temperatures above 100 °C. This is because the pre-straining has been applied at room temperature (RT) rather than at the test temperatures and the effectiveness of the pre-strain induced defects depends on test temperature.

4.2. Equivalent fracture stress and fracture strain

In Fig. 5, the ends of the equivalent true stress–true strain curves were considerably varied with test temperature for all tested materials. This implies that the equivalent fracture stress and fracture strain of austenitic stainless steels are strongly dependent on the test temperature. Fig. 7 shows the variations of equivalent fracture stress for all materials with test temperature, together with yield stress (σ_{YS}) and plastic instability stress (σ_{PIS}) given by previous study [20]. It was shown that overall temperature dependence of σ_{FE} for each material resembles that of σ_{PIS}; it decreased rapidly with test temperature in the temperature range <200 °C and saturated at an athermal stress level above 200 °C. However, the equivalent fracture stress was more sensitive to the test temperature than the plastic instability stress; the reduction in σ_{FE} with test temperature was steeper. Thus, the σ_{FE} was approximately twice the σ_{PIS} at temperatures below 100 °C, while the difference between σ_{FE} and σ_{PIS} became minor above 200 °C even though the difference between σ_{YS} and σ_{PIS} was still considerable except for the 20% CW 316LN SS. The difference between the equivalent fracture stresses of test materials became more obvious as the temperature decrease below RT. The highest and lowest of σ_{FE} are observed in the annealed 304 SS and annealed 316LN SS, respectively. Such difference was reduced significantly at elevated temperature. Fig. 7 also shows that the values of σ_{FE} for the 20% CW 316LN SS are almost the same as those for the

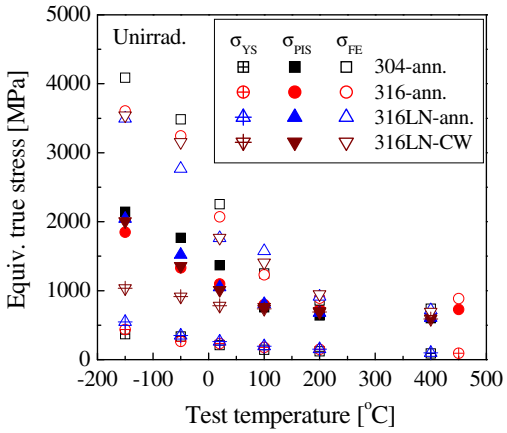

Fig. 7. Temperature dependence of equivalent true stress parameters for annealed 304, 316, 316LN, and 20% CW 316LN stainless steels.

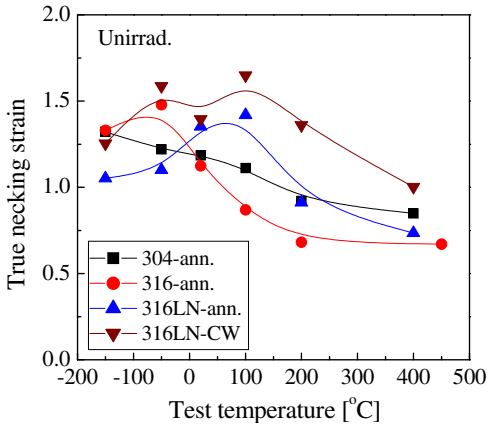

Fig. 9. Temperature dependence of necking strains for annealed 304, 316, 316LN, and 20% CW 316LN stainless steels.

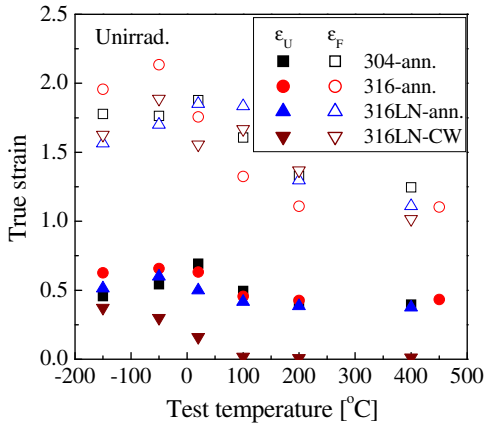

Fig. 8. Temperature dependence of equivalent true strain parameters for annealed 304, 316, 316LN, and 20% CW 316LN stainless steels.

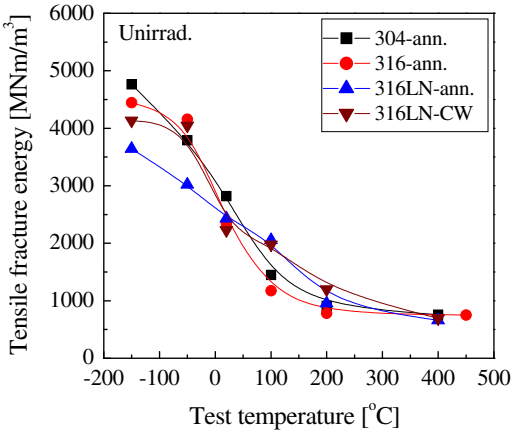

Fig. 10. Temperature dependence of tensile fracture energies for annealed 304, 316, 316LN, and 20% CW 316LN stainless steels.

annealed 316LN SS. This indicates that the equivalent fracture stress is independent of pre-straining, as is observed in strain hardening behavior.

Fig. 8 presents the equivalent fracture strain (ε_F) data plotted against temperature, along with the true uniform strain (ε_U). The ε_F increased with temperature in the low temperature range, reached a maximum at −50 °C to 20 °C, and then rapidly decreased to 1.1–1.4 at 200 °C. Above 200 °C, the values of ε_F were retained at 1.0–1.3, which are about half of the maximum values. For each material, the temperature dependence of fracture strain is similar to that of true uniform strain, although the variation of ε_F over a temperature change is larger than that of ε_U. Below RT the ε_F for annealed 316 SS was higher than those for the other materials, however, it rapidly decreased with temperature and became the lowest above 100 °C. In this material the critical temperature at which the fracture strain starts to decrease with temperature was lower compared to the other materials.

The true necking strain ($\Delta\varepsilon_n$), which is defined by the difference between ε_F and ε_U and plotted in Fig. 9, tends to have a maximum below ~100 °C and decreased with temperature. Over the test temperature range the 20% CW 316LN SS showed similar or higher necking strain than the annealed austenitic stainless steels including the 316LN SS. This result indicates that pre-straining does not reduce the ductility of unstable deformation under a multi-axial loading condition.

4.3. Tensile fracture energy

Since the full equivalent true stress–true strain curves including unstable deformation were produced in this study, the tensile fracture energy (E_F), which is a measure of toughness for low constraint, was able to be calculated using those curves. Here, the E_F was defined by an area of full equivalent true stress–true strain curve, as given by Eq. (7):

$$E_F = \int_0^{\varepsilon_F} \sigma_T d\varepsilon_T. \tag{7}$$

Fig. 10 presents the E_F as a function of test temperature. The E_F value decreased rapidly with test temperature below 200 °C; the values of E_F at −150 °C were about 3–4 times higher than those at 200 °C. This overall temperature dependence is similar to that of σ_{FE} shown in Fig. 7, while the material dependence was more obvious in the E_F values. At low temperatures, −150 and −50 °C, the annealed 304 SS and 316 SS showed the highest E_F and the annealed 316LN SS the lowest. It is notable that the E_F of the 20% CW 316LN SS is similar to those of the annealed 304 and 316 SS, although it experienced prompt necking at yield above RT. The temperature dependence of tensile fracture energy agrees with that of fracture toughness in austenite stainless steels in ductile region [22], where the resistance to ductile failure decreased

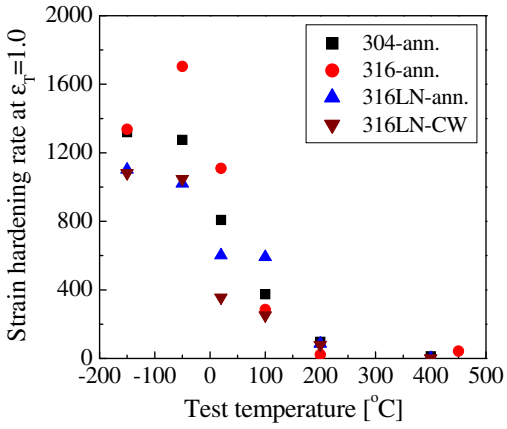

Fig. 11. Temperature dependence of strain hardening rate at $\varepsilon_T = 1$ for annealed 304, 316, 316LN, and 20% CW 316LN stainless steels.

rapidly with temperature. Among the test materials the temperature dependence of the fracture resistance was most profound in the annealed 316 SS.

4.4. Discussion on the temperature dependence of fracture properties

The present results indicate that the equivalent fracture stress, fracture strain, and tensile fracture energy are more sensitive to the test temperature compared to the temperature dependences of plastic instability stress and uniform strain, which are based on uniform deformation. As temperature increased, these properties steeply decreased and nearly saturated above 200 °C. This temperature dependence in the fracture properties is related to the rapid decrease in the strain hardening capability beyond the onset of necking at elevated temperature, as shown in Fig. 11, which may be attributed to the change in strain hardening mechanism at high strain region of austenitic stainless steels with test temperature.

In general, the deformation mode of face centered cubic material gradually changes from highly planar slip to cross slip inducing more tangles as strain increases, and the saturation of dislocation tangle can result in exhaustion of strain hardening capability of material. Especially in the low stacking fault energy (SFE) materials such as the present austenitic stainless steels, the mechanical twining mechanism and martensitic transformation as well as planar slip system are activated during plastic deformation and they often enhance hardening capability [10,20,23]. Since the mechanical twining and strain induced martensite are equivalent to a progressive formation of obstacles, they supply less exhaustible hardening mechanism than dislocation tangling [20]. Thus, the strain hardening capability is sustained to relatively high strain region, when these deformation systems are activated for plastic deformation in austenitic stainless steels. Previous study showed that the strain induced martensite is generated at low temperatures of −150 and −50 °C for austenitic stainless steels [20], and mechanical twinning system is activated at test temperature below about 200 °C for austenitic stainless steels [10,20,23]. It is believed therefore that the high strain hardening rate maintained beyond the onset of necking at low test temperatures of −150 and −50 °C is associated with the activation of mechanical twinning and often martensite in addition to the planar slip during plastic deformation.

The high strain hardening rate can homogenize plastic deformation over the gage section of specimen, and consequently results in high fracture strain and fracture stress as well as high uniform strain. In the temperature range of RT −200 °C, activation and operation of mechanical twinning and planar slip systems are believed to be the major contributors to plastic flow and strain hardening [10,20,23]. At low temperature the activation of twinning system is easy due to its relatively low stacking fault energy (SFE), and thus its effect dominates in the deformation of stainless steels. However, the critical stress for dislocation glide decreases with temperature, while the critical stress for mechanical twinning increases slowly. Thus, planar slip becomes more important than mechanical twinning and governs plastic flow at elevated temperatures [23]. With increasing test temperature, also, the increased SFE in the austenitic steels results in more cross-slips even at low strain, so that the strain hardening by dislocation tangle is saturated at relatively early stage of plastic deformation [24]. In the temperature range of RT ∼ 200 °C, therefore, the rapid decrease in strain hardening capability beyond the onset of necking with test temperature is because the contribution of planar slip gradually increases in early stage and it changes to cross-slip at relatively low strain. Further, a higher dislocation interaction should leads to a higher rate of thermal dislocation annihilation at elevated temperatures. Such a reduced strain hardening capability during unstable deformation results in the rapid decrease in the equivalent fracture stress, fracture strain, and tensile fracture energy. Above 200 °C, the activation of mechanical twinning is nearly absent but planar slip system is operated [23]. Since the dislocation tangles by cross-slip contributes more to strain hardening of austenitic stainless steels in this temperature range, the strain hardening capability is almost exhausted during uniform deformation and negligible at high strain region beyond the onset of necking. Therefore, the fracture properties reach the minimum values and are unchanged in this temperature region.

On the other hand, at temperatures above RT the annealed 316 SS showed lower equivalent fracture stress, fracture strain, and tensile fracture energy compared to other tested materials including 20% CW 316LN SS. It was also shown that these properties for annealed 316 SS steeply decreased with increasing test temperature. This may be related to relatively higher SFE of annealed 316 SS than those of other test materials [3,6,24]. As discussed above, high SFE delays the activation of mechanical twinning of austenitic stainless steels and promotes the transition from planar slip to cross slip at early deformation stage. In annealed 316 SS with relatively high SFE, the saturation of strain hardening capability would appear at lower strain region and at lower test temperature compared to annealed 304 SS and 316LN SS. Therefore, the values of fracture parameters influenced by strain hardening capability during unstable deformation steeply decreased and became lower in the elevated temperature region. This also explains why the differences of fracture properties among the materials become minimal above 200 °C, where the dislocation tangling, which should be accompanied by annihilation due to interactions, becomes a common strain hardening mechanism for all test materials.

5. Conclusions

Full-range equivalent true stress–true strain curves were determined for annealed 304, 316, and 316LN and 20% cold-worked (CW) 316LN using an iterative finite element simulation technique. Discussions were made focusing on the temperature dependence of strain hardening behavior in unstable deformation and fracture properties, and the following conclusions were drawn:

(1) In the austenitic stainless steels relatively high strain hardening rate was retained during unstable deformation. However, the strain hardening capability at elevated temperatures was relatively low because dislocation tangling with annihilation became dominant.

(2) In all tested materials including 20% CW 316LN SS the equivalent fracture stress and tensile fracture energy decreased rapidly with temperature in the low temperature range <200 °C and nearly saturated at higher temperatures up to 450 °C.
(3) As temperature increased, the fracture strain peaked at −50 to 20 °C, depending on material, and then rapidly decreased until the temperature reached about 200 °C. Above 200 °C, the values of fracture strain retained at 1.0–1.3, which were approximately 50% of the maximum values.
(4) The effects of pre-straining on the strain hardening rate beyond the onset of necking, equivalent fracture stress, fracture strain, and tensile fracture energy were not significant at all test temperatures.
(5) Among the tested materials, annealed 316 SS showed the lowest equivalent fracture stress, fracture strain, and tensile fracture energy at temperatures above RT. This may be attributed to the relatively higher stacking fault energy of the annealed 316 SS.

Acknowledgements

This study was supported by the research funds of Chosun University in Korea and was a continuation of the earlier studies sponsored by US Department of Energy, Offices of Fusion Energy Sciences and Basic Energy Science, under Contract DE-AC05-00OR22725 with UT-Battelle, LLC. The authors express special thanks to Drs. John G. Merkle and C.S. Shin for their technical reviews and thoughtful comments.

References

[1] T.S. Byun, K. Farrell, Acta Mater. 52 (2004) 1597.
[2] E.I. Samuel, B.K. Choudhary, K.B.S. Rao, J. Nucl. Mater. 480 (2008) 506.
[3] T.S. Byun, K. Farrell, M. Li, Acta Mater. 56 (2008) 1044.
[4] G.R. Odette, M.Y. He, E.G. Donahue, G.E. Lucas, In Small Specimen Test Technique: Fourth Volume, ASTM STP 1418, ASTM International, West Conshohocken, PA, 2002. p. 221.
[5] Y. Dai, G.W. Egeland, B. Long, J. Nucl. Mater. 377 (2008) 109.
[6] T.S. Byun, N. Hashimoto, Nucl. Eng. Tech. 38 (2006) 619.
[7] P.W. Bridgeman, Studies in Large Plastic Flow and Fracture, McGraw-Hill, New York, 1952.
[8] V.V. Toropov, F. Yoshida, E. Van der Giessen, in: Proceedings of the Euromech Colloquium, Kluwer Academic Publishers, Kerkrade, The Netherlands, 1997. p. 81.
[9] Y. Ling, AMP J. Technol. 5 (1996) 37.
[10] T.S. Byun, N. Hashimoto, K. Farrell, J. Nucl. Mater. 351 (2006) 303.
[11] T.S. Byun, J. Nucl. Mater. 361 (2007) 239.
[12] T.S. Byun, M. Li, B.V. Cockeram, L.L. Snead, J. Nucl. Mater. 376 (2008) 240.
[13] W.D. Callister Jr., Materials Science and Engineering: An Introduction, sixth ed., John Wiley and Sons, Inc., 2003.
[14] Y. Bao, Eng. Frac. Mech. 72 (2005) 502.
[15] C.K. Oh, Y.J. Kim, J.H. Baek, W.S. Kim, Int. J. Fract. 143 (2008) 119.
[16] P. Koc, B. Stok, Comp. Mater. Sci. 31 (2004) 155.
[17] V. Tvergaard, Comp. Methods Appl. Mech. Eng. 103 (1993) 273.
[18] K. Ikeda, S. Okazawa, K. Terada, H. Noguchi, T. Usami, Int. J. Eng. Sci. 39 (2001) 1913.
[19] M. Joun, J.G. Eom, M.C. Lee, Int. J. Mech. Mater., in press doi:10.1016/j.mechmat.2007.11.006.
[20] T.S. Byun, N. Hashimoto, K. Farrell, Acta Mater. 52 (2004) 3889.
[21] ABAQUS Ver. 6.5 User's Manual, Hibbitt, Karlson, and Sorensen Inc., 2005.
[22] S.A. Maloy, M.R. James, G. Willcutt, W.F. Sommer, M. Sokolov, L.L. Snead, M.L. Hamilton, F. Garner, J. Nucl. Mater. 296 (2001) 119.
[23] X. Wu, X. Pan, J.C. Mabon, M. Li, J.F. Stubbins, J. Nucl. Mater. 356 (2006) 70.
[24] B.K. Choudhary, E.I. Samuel, K.B.S. Rao, S.L. Mannan, Mater. Sci. Technol. 17 (2001) 223.